

Efficient implementation of x-ray ghost imaging based on a modified compressive sensing algorithm

Haipeng Zhang(张海鹏), Ke Li(李可), Changzhe Zhao(赵昌哲), Jie Tang(汤杰), and Tiqiao Xiao(肖体乔)
Citation: Chin. Phys. B, 2022, 31 (**6**): 064202. DOI: 10.1088/1674-1056/ac48f7
Journal homepage: http://cpb.iphy.ac.cn; http://iopscience.iop.org/cpb

What follows is a list of articles you may be interested in

Color-image encryption scheme based on channel fusion and spherical diffraction

Jun Wang(王君), Yuan-Xi Zhang(张沅熙), Fan Wang(王凡), Ren-Jie Ni(倪仁杰), and Yu-Heng Hu(胡玉衡)
Chin. Phys. B, 2022, 31 (**3**): 034205. DOI: 10.1088/1674-1056/ac1b87

Refocusing and locating effect of fluorescence scattering field

Jian-Gong Cui(崔建功), Ya-Xin Yu(余亚鑫), Xiao-Xia Chu(楚晓霞), Rong-Yu Zhao(赵荣宇), Min Zhu(祝敏), Fan Meng(孟凡), and Wen-Dong Zhang(张文栋)
Chin. Phys. B, 2021, 30 (**12**): 124210. DOI: 10.1088/1674-1056/ac2804

Computational ghost imaging with deep compressed sensing

Hao Zhang(张浩), Yunjie Xia(夏云杰), and Deyang Duan(段德洋)
Chin. Phys. B, 2021, 30 (**12**): 124209. DOI: 10.1088/1674-1056/ac0042

High speed ghost imaging based on a heuristic algorithm and deep learning

Yi-Yi Huang(黄祎祎), Chen Ou-Yang(欧阳琛), Ke Fang(方可), Yu-Feng Dong(董玉峰), Jie Zhang(张杰), Li-Ming Chen(陈黎明), and Ling-An Wu(吴令安)
Chin. Phys. B, 2021, 30 (**6**): 064202. DOI: 10.1088/1674-1056/abea8c

A fast and precise three-dimensional measurement system based on multiple parallel line lasers

Yao Wang(王尧) and Bin Lin(林斌)
Chin. Phys. B, 2021, 30 (**2**): 024201. DOI: 10.1088/1674-1056/abc14d

---

Efficient implementation of x-ray ghost imaging based on a modified compressive sensing algorithm

Haipeng Zhang(张海鹏)[1,2,3], Ke Li(李可)[2], Changzhe Zhao(赵昌哲)[1,2,3], Jie Tang(汤杰), and Tiqiao Xiao(肖体乔)[1,2,3,†]

[1] *Shanghai Institute of Applied Physics, Chinese Academy of Sciences, Shanghai* 201800, *China*
[2] *Shanghai Synchrotron Radiation Facility/Zhangjiang Laboratory, Shanghai Advanced Research Institute, Chinese Academy of Sciences, Shanghai* 201204, *China*
[3] *University of Chinese Academy of Sciences, Beijing* 100049, *China*

(Received 22 September 2021; revised manuscript received 2 January 2022; accepted manuscript online 7 January 2022)

Towards efficient implementation of x-ray ghost imaging (XGI), efficient data acquisition and fast image reconstruction together with high image quality are preferred. In view of radiation dose resulted from the incident x-rays, fewer measurements with sufficient signal-to-noise ratio (SNR) are always anticipated. Available methods based on linear and compressive sensing algorithms cannot meet all the requirements simultaneously. In this paper, a method based on a modified compressive sensing algorithm with conjugate gradient descent method (CGDGI) is developed to solve the problems encountered in available XGI methods. Simulation and experiments demonstrate the practicability of CGDGI-based method for the efficient implementation of XGI. The image reconstruction time of sub-second implicates that the proposed method has the potential for real-time XGI.

Keywords: x-ray ghost imaging, modified compressive sensing algorithm, real-time x-ray imaging

PACS: 42.30.Va, 42.30.Wb **DOI:** 10.1088/1674-1056/ac48f7

1. Introduction

Correlation imaging, also known as ghost imaging (GI), is a novel non-localized imaging method that has attracted widespread attention and investigation during the recent years.[1–4] Combined with the lensless GI technology,[5–7] x-ray ghost imaging (XGI) has the advantage of high spatial resolution,[8–10] deep penetration, high sensitivity and potentially low radiation dose.[11,12] In order to break the resolution limit of the detector to explore more subtle structure, Yu *et al*. experimentally demonstrated the reconstruction of both the amplitude and phase of a multi-slits sample with the slit width smaller than the pixel size using Fourier-transform XGI.[2] So far, these superiorities of XGI[2,13–15] have made it gradually flourish in biomedicine and material science.

Towards the practical applications of XGI, especially for biomedical imaging to live organisms *in vivo* and clinical diagnosis, it is indispensable to achieve XGI with high efficiency which is reflected on efficient data acquisition and fast image reconstruction[16–18] together with high image quality. The data acquisition time is determined by the refreshing frequency of the modulating mask[19] and the required number of measurements to ensure reconstruction of high fidelity. Computational XGI[20] provides a feasible solution in reducing the data acquisition time. As long as the intensity distribution of the chaotic x-ray source can be pre-recorded[12] or calculated,[20] signals containing sample information can be quickly collected through rotating the mask which can accelerate the refreshing rate. Moreover, some other strategies including splitting x-ray beams based on crystal diffraction[13,14] were proposed for the efficient implementation of XGI to evade the tedious switch of samples in and out of a single x-ray beam.[2] Since these signals in the object arm are registered by a barrel detector with extremely high sensitivity and low exposure time, it is theoretically possible to achieve ultra-low acquisition time for per measurement. In addition, reducing the number of measurements under the premise of high image quality can further shorten the data acquisition time and diminish the radiation dose imposed on the object. At present, compressive sensing (CS) techniques utilizing the sparse prior have been a credible choice to recover high-quality 'ghost' images with fewer measurements.

Since Katz *et al*.[21] put forward compressive ghost imaging (CGI) which exploited the redundancy in the structure of natural images, CS has been prevalent in single-pixel imaging. According to sparsity constraints, CGI can restore high-fidelity images with the number of measurements much less than Nyquist–Shannon criterion. Correspondingly, the data acquisition time required for a high-quality reconstruction is also dramatically reduced. In addition, fewer measurements can simultaneously speed up the reconstruction for different algorithms. Furthermore, CGI breaks the limitation that the resolution of the recovered image is determined by the size of speckles in the reference patterns in the traditional GI. However, CS techniques are confronted with an inherent problem

†Corresponding author. E-mail: xiaotiqiao@zjlab.org.cn
© 2022 Chinese Physical Society and IOP Publishing Ltd

that high-performance reconstruction by CS usually means an increase in iterations, which results in huge computational cost or long reconstruction time (RT) and prevent CGI from real-time imaging. Hence, the measurement number and RT maintain the major stumbling obstacle towards real-time XGI with high quality and efficient image reconstruction. In the visible light regime, the irrelevant speckle patterns devised by spatial light modulator (SLM) combined with the matching algorithms can obviously speed up the reconstruction.[22] Suitable optics such as SLM have not yet been found to modulate the devised speckle patterns in x-ray regime. Accordingly, in the algorithm framework suitable for universal situations, a method based on a modified compressive sensing algorithm with conjugate gradient descent method (CGDGI) is proposed to retrieve 'ghost' images rapidly and robustly while ensuring the reconstruction quality with few measurements and iterations, aiming at efficient implementation of XGI concerning the data acquisition and image reconstruction.

2. Principle

Different from traditional GI[14] using ensemble average on intensity correlation, differential ghost imaging (DGI) presented by Ferris *et al.*[23] substitutes the total intensity with the differential bucket signal, which is sensitive to intensity fluctuation and can suppress background noise. As a result, DGI can effectively extract the spatial information of the object with higher signal-to-noise ratio (SNR). The formula for DGI is described as following:

$$G^{(2)}_{\mathrm{DGI}}(p,q) = \langle I_i(p,q)S_i\rangle - \frac{\langle S_i\rangle}{\langle R_i\rangle}\langle I_i(p,q)R_i\rangle, \tag{1}$$

where $I_i(p,q)$ and S_i respectively represent the reference patterns recorded by spatially resolved detector and the total intensity collected by the single-pixel detector during the i-th realization. $R_i = \sum_{p,q} I_i(p,q)$ denotes the total intensity on the i-th reference pattern, $i = 1,2,\ldots,M$, and M implies the total number of measurements. The angle bracket $\langle\cdot\rangle$ denotes the ensemble average over all the measurements.

The image obtained by DGI does not completely satisfy the inherent constraint $S_i = \sum_{p,q} I_i(p,q)\,T(p,q)$, where $T(p,q)$ denotes the transmittance or reflectance of the intensity at the pixel location (p,q) in the object plane. Moreover, due to the background noise, the reconstructed image by DGI usually violates the prior that the gradient of natural images is sparse. Therefore, on the basis of DGI result which is relatively close to the ground truth, total variation (TV) regularization[24] is utilized to iteratively converge and satisfy the sparse prior and inherent constraint simultaneously, which is expected to further ameliorate the DGI image. In addition, the isotropic TV term frequently used in the algorithm results in fewer zig-zagging boundaries in reconstruction. However, the non-differentiability and non-linearity of TV function make the solution more complicated than greedy algorithms[25] or l_1 minimization[26] and cost much more data processing time. In the modified CS algorithm, the square of the isotropic TV term is selected as the new regularization term, and the corresponding mathematical model is established as following:

$$T_{\mathrm{CGDGI}} = \min TV^2(T) \text{ subject to } S = AT, \tag{2}$$

where $A \in R^{M\times N}$ means the measurement matrix composed of M reference patterns with the size of $N = N_1 \times N_2$, $S \in R^{M\times 1}$ denotes the observation vector consisted with M signals collected from the bucket detector, where each element is S_i, and T_{CGDGI} represents the image to be restored by CGDGI and

$$\begin{aligned} TV^2(T) &= \sum_{p,q}[T(p+1,q) - T(p,q)]^2 \\ &\quad + [T(p,q+1) - T(p,q)]^2. \end{aligned} \tag{3}$$

Equation (2) can be solved by the equivalent unconstrained problem given as

$$\min_T Q(T) = \frac{\lambda}{2}\|AT - S\|_2^2 + \frac{1}{2}TV^2(T), \tag{4}$$

where λ denotes the penalty coefficient to compromise the regularization term and fidelity term. Generally, λ is set to be a smaller value to adapt to higher noise. As the regularization term, $TV^2(T)$ is also isotropic and inherits the superiority that preserves the clarity of the edges.

Due to that $Q(T)$ is the quadratic function of T, conjugate gradient descent (CGD) can be used to achieve fast convergence. Theoretically, CGD selects the global optimal descent direction to speed up convergence, so sufficient accuracy can be achieved through finite iterations. The gradient $g(T) = \partial Q(T)/\partial T = HT + C$ can be obtained simply by firstly calculating Hessian matrix H and the corresponding constant C, as shown below:

$$H = \frac{\partial^2 Q}{\partial^2 T} = \lambda A'A + 4E, \tag{5a}$$

$$C = -\lambda A'S, \tag{5b}$$

where the superscript $'$ denotes the transpose and E is a constant matrix determined merely by the image size of $N_1 \times N_2$. Simplified calculation aims at shortening RT. The global optimal descent direction d, known as the conjugate gradient descent direction, can be obtained through

$$d_{k+1}(T) = g_{k+1}(T) + \frac{g'_{k+1}(T)g_{k+1}(T)}{g'_k(T)g_k(T)}d_k(T), \tag{6}$$

where $d_k(T)$ and $g_k(T)$ represent respectively the gradient and conjugate gradient in the k-th iteration. The specific flow chart of CGDGI algorithm is shown as follows.

The flow chart of CGDGI algorithm.

1	Initialize λ, ε and the maximum iteration steps K	Annotations
2	Calculate G_{DGI} according to DGI algorithm, and $T_{(0)} = G_{\mathrm{DGI}}$	$T_{(k)}$ is the image to be reconstructed in the k-th iteration
3	Calculate $H = \partial^2 Q/\partial^2 T$ and $h = \partial Q/\partial T - HT$	H, h are constants
4	Firstly $k = 0$, $g_{(0)} = HT_{(0)} + h$, $d_{(0)} = g_{(0)}$,	
5	While $k < K$ & $d_{(k)} < \varepsilon$	
	$\alpha_{(k)} = g'_{(k)} d_{(k)} / (d'_{(k)} H d_{(k)})$	
	$T_{(k+1)} = T_{(k)} - \alpha_{(k)} d_{(k)}$	The superscript $'$ denotes transpose
	$g_{(k+1)} = HT_{(k+1)} + h$	
	$d_{(k+1)} = g_{(k+1)} + g'_{(k+)} g_{(k+1)} / (g'_{(k)} g_{(k)}) d_{(k)}$	
	$k \leftarrow k+1$	
	end	
6	Return the last outcome $T_{(K)}$	

Different from the total variation minimization by augmented Lagrangian and alternating direction algorithm (TVAL3),[24] CGDGI accelerates the reconstruction by solving the main equation (Eq. (4)) in only a single loop. It is obvious that CGDGI with a single loop structure can run much quicker than TVAL3 with a nested loop structure. Moreover, CGDGI can achieve higher convergence precision to obtain better reconstruction with limited iterations through conjugate gradient descent method, so that CGDGI is expected to reconstruct high-fidelity images robustly and efficiently through few iterations based on the DGI result as the initial input of the iterations in CGDGI. The simplicity of DGI can save much RT for CGDGI. The algorithm metrics including RT, peak signal-to-noise ratio (PSNR),[27] structural similarity (SSIM)[28] index and meta-rate (MR)[29] are utilized to evaluate performances of the proposed algorithm in comparison to other classical algorithms.

3. Results and analysis

3.1. Simulation

To demonstrate the effectiveness of CGDGI proposed in the paper, a numerical simulation is carried out prior to experiments. Different algorithms are adopted to provide a comparison for CGDGI including typical linear algorithms such as iterative denoising of ghost imaging (IDGI),[30] pseudo-inverse ghost imaging (PGI),[31] and classical CS algorithms such as orthogonal matching pursuit (OMP),[25] basis pursuit denoising (BPDN)[26] and TVAL3.[24] The schematic diagram for the simulation is sketched in Fig. 1, which is similar to that in Ref. [2]. In the numerical simulation, the pseudo-thermal x-ray source is artificially generated by a sandpaper acting as masks illuminated by a monochromatic x-ray beam collimated by an aperture. The object was mounted a distance d_1 downstream the sandpaper and followed by a panel detector a distance d_2 away from the object. Theoretically, d_2 should be set as zero to meet the confocal condition of real-space XGI that the distance from source to object is equal to that from source to the panel detector. However, the defocused distance $d_2 \neq 0$ is inevitable in this scheme of actual situations. In the simulation, d_2 is set as 0.5 cm $\ll d_1 = 45$ cm to conform actual situations without excessively violating the confocal condition. The reference patterns and object signals are respectively registered through shuttling the object into and out of the beam. The reference patterns of stochastic speckles are produced by the propagation of the field modulated by randomly distributed irregular particles based on inference of the randomly scattered radiation. The full width at half maximum (FWHM) of the autocorrelation function for all the reference patterns is 5 pixels, and its maximum is approximately 1.95. The larger the maximum of the autocorrelation function which represents the fluctuation degree of the speckle intensity, the higher efficiency and fidelity 'ghost' images can be retrieved.[33] On the other hand, the object signals are also recorded by the same panel detector which integrates the total intensity all over the pixels as a bucket detector.

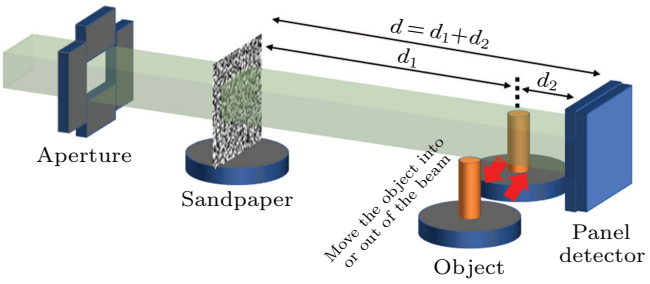


Fig. 1. Schematic diagram of experimental setup. The object is toggled in or out of the x-ray beam to record bucket signals and reference patterns respectively.

In order to verify the robustness of CGDGI for reconstruction of objects with complex structures, the grayscale image 'Lena' with 64×64 pixels is employed as the target image in numerical simulation, with additive Gaussian white noise of different strengths. In the simulation, noise is directly added to the speckle patterns and the bucket signals that contain the object information, as shown in following:

$$I_i^{\mathrm{N}}(p,q) = I_i(p,q) + N_i^{\mathrm{R}}(p,q), \tag{7a}$$

$$S_i^{\mathrm{N}} = \sum_{p,q} T(p,q) I_i(p,q) + N_i^{\mathrm{O}}(p,q), \tag{7b}$$

where $I_i^{\mathrm{N}}(p,q)$ indicates the speckle patterns with Gaussian white noise N_i^{R} in the reference arm and S_i^{N} implies the bucket signal contaminated by the noise N_i^{O} in the object arm during the i-th realization. N_i^{O} obeys the same probability distribution as N_i^{R}, since both of them are introduced by the same detector. The superscript N indicates that the raw data $I_i^{\mathrm{N}}(p,q)$ and S_i^{N} are noisy. The superscripts R and O represent the noise N_i in the reference arm and the object arm, respectively. The strength of noise is represented by the mean μ_{N} and the standard deviation σ_{N}. Generally, the fluctuation of the standard deviation can well describe the noise strength. Accordingly, noise with different standard deviations is introduced in the simulation to demonstrate the robustness of the algorithms.

According to the common experience, the reconstruction quality and RT of CGDGI will increase with the growing number of measurements. As shown in Fig. 2, both PSNR and RT gradually grow with the iteration number and the measurements at different noise level. However, the growth rate of PSNR slows down significantly when the iteration number exceeds 10 and the measurements surpass 600 despite of different noise level, as shown in Figs. 2(a) and 2(b). SNR is an explicit index to evaluate the noise level. Therefore, according to the definition of SNR, SNR for the reference speckle patterns contaminated by noise with the mean μ_{N} and the standard deviation σ_{N} is derived as

$$\mathrm{SNR} = 10\log_{10}\left(\frac{\mu_{\mathrm{s}}^2 + \sigma_{\mathrm{s}}^2}{\mu_{\mathrm{N}}^2 + \sigma_{\mathrm{N}}^2}\right), \tag{8}$$

where μ_{s} and σ_{s} ($\sigma_{\mathrm{s}} = \mu_{\mathrm{s}}$) indicate the mean and the standard deviation of the negative exponential distribution obeyed by the reference speckle patterns. The average intensity μ_{s} of the speckle patterns is approximately 8984, so the Gaussian noise with the mean $\mu_{\mathrm{N}} = 100$ and the standard deviation $\sigma_{\mathrm{N}} = 10$, 50, 100 is converted into SNRs of 42.0 dB, 41.1 dB, 39.1 dB, respectively. The values of the parameter λ is set to 46, 42 and 39 respectively to obtain the optimal images under the above-mentioned environments with different noise level.

While under the circumstances of different measurements, PSNR's rising tendency also slows down when the iteration number is larger than 10, as shown in Fig. 2(c). In the other hand, RT also increases with the more measurements which constitute a larger measurement matrix, as shown in Fig. 2(d). Therefore, a suitable number of both iterations and measurements should be chosen carefully. The iteration number for further simulation is set to 10 and the measurement number M is set to approximately 600 to ensure efficient image reconstruction under the premise of high fidelity. Certainly, the conclusion is also instructive for the subsequent experiments.

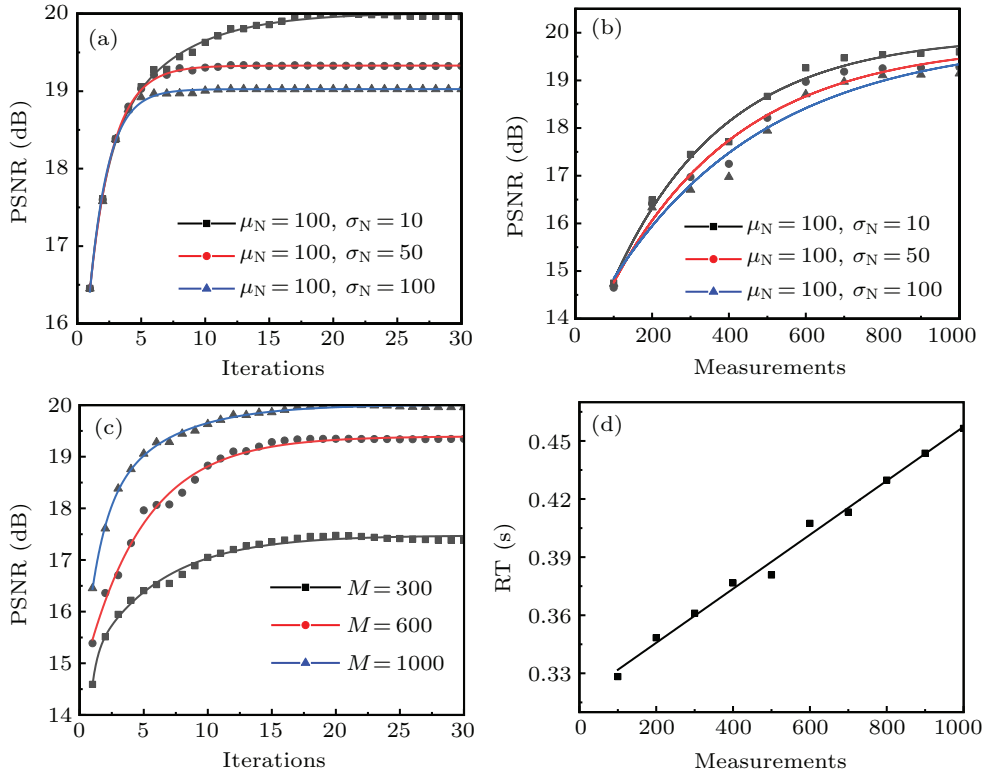


Fig. 2. Numerical simulation of 'Lena' with PSNR and RT varying with the iteration and measurement number, where (a) PSNR vs. iterations with measurement number of M set to 1000, noise's mean $\mu = 100$ and standard deviation $\sigma = 10$, 50, 100 respectively, (b) PSNR vs. measurements with the iteration set to 10, noise $\mu = 100$ and $\sigma = 10$, 50, 100 respectively, (c) PSNR vs. iteration with measurements set to 300, 600, 1000 respectively, and (d) RT vs. measurements when the iteration number is set to 10 according to the conclusion of (a) and (c).

Lena reconstructed by different algorithms under the noise levels with $\mu_N = 100$ and $\sigma_N = 10$ are displayed in Fig. 3. The measurement number M is set to 600, and the images stand for target (a), DGI (b), IDGI (c), PGI (d), OMP (e), BPDN (f), TVAL3 (g) and CDGGI (h), respectively. From the visual perspective, these images retrieved by linear algorithms listed above merely exhibit the blurred outlines but lose the tiny details, as shown in Figs. 3(c) and 3(d). Moreover, the IDGI image, looks evidently worse than the DGI image as shown in Fig. 3(c). This was also demonstrated by PSNR in which value for IDGI was 14.98 dB smaller than 15.36 dB for DGI. Although the IDGI image is originally expected to be ameliorated through several iterations after DGI, the result is not satisfactory due to the complex structure and relatively low contrast in Lena. Compared with CGDGI, IDGI not only spends as nearly twice time but also recovers an image far worse under the computer configuration intel (R) Core (TM) i9-9900K CPU @3.60 GHz. As shown in Fig. 3(d), the random 'salt and pepper' throughout the whole image severely deteriorate the PGI image which merely reproduces the blurred morphology of Lena. As well known, PGI is vulnerable to environmental noise, which results in a poor PSNR. The poor noise resistance of PGI will be further proved in the following experiments. In addition, PGI spends nearly half more time for reconstruction than CGDGI. In summary, for all the typical linear algorithms, based on the explicit observation low image quality were achieved even though the image reconstruction time is quite limited. This implicates that it is hard to achieve high image quality and efficient reconstruction with linear algorithms.

In CS algorithms such as OMP and BPDN, discrete cosine transform (DCT) is selected as an appropriate sparse basis and the parameters are optimized to achieve the best reconstruction in all kinds of CS algorithms. The images reconstructed by CS algorithms were generally of higher fidelity than that by linear algorithms, as shown in Fig. 3. However, the fidelity improvement for CS algorithms is at the expense of significantly increased time consumption. As shown in Fig. 3(e), the raindrop-like artifacts all over the image severely degrade the quality of Lena reconstructed by OMP, which limits its practical application in noisy scenes. As shown in Fig. 3(f), BPDN based on DCT basis still cannot evidently eliminate the artifacts and will not distinguish the Lena's facial contour clearly. However, RT of 9.44 s for BPDN is much longer than that of around half a second for the linear algorithms. Based on the property that the gradient of natural images is sparse, TVAL3 depicts more accurately the sparsity of Lena, and the reconstruction by TVAL3 looks smoother as shown in Fig. 3(g). Relative to BPDN, the RT for TVAL3 is reduced to 6.28 s. The image quality for TVAL3 is sufficiently high but the relatively long reconstruction time cannot still meet the requirements of an efficient XGI. CGDGI is proposed to improve the reconstruction efficiency of BPDN and TVAL3. As shown in Fig. 3(h), Lena recovered by CGDGI reveals the structure details with higher contrast especially textures on the hat. While the image quality of CGDGI is comparable to that of BPDN and TVAL3, and the RT is significantly reduced to 0.4 s. Considering the image acquisition time needed for all the measurements, the subsecond RT of CGDGI can ensure the efficient implementation of XGI. Certainly, for samples with simpler structure than Lena, the requirements for measurement number can be greatly reduced and accordingly the efficiency for data acquisition in CGDGI is improved significantly. As a result, CGDGI based XGI with efficiency data acquisition and image reconstruction is anticipated.

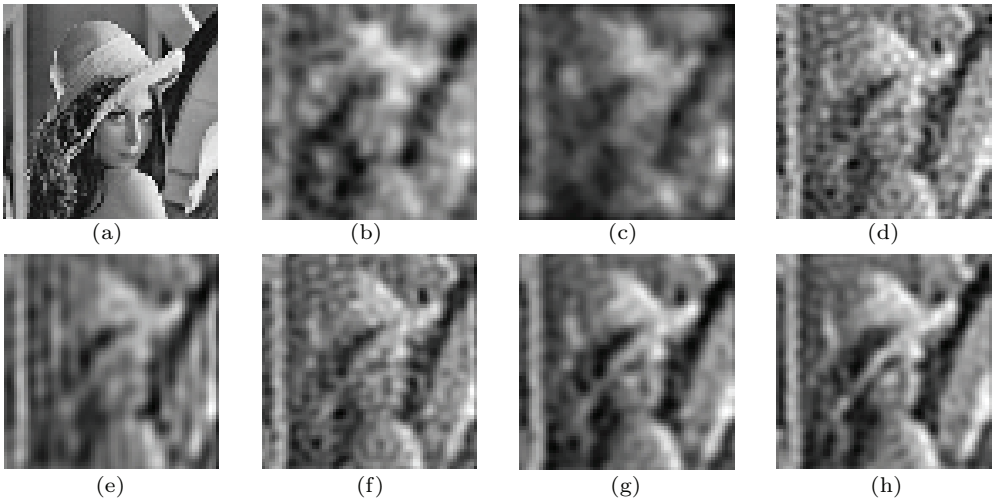


Fig. 3. Lena reconstructed by various algorithms under the noise level with $\mu_N = 100$ and $\sigma_N = 10$ and the measurement number $M = 600$, where (a) target image. (b) DGI with RT of 0.02 s and PSNR of 15.36 dB, (c) IDGI with RT of 0.55 s and PSNR of 14.98 dB, (d) PGI with 0.54 s and 17.79 dB, (e) OMP with 0.84 s and 17.6 dB, (f) BPDN with 9.44 s and 18.51 dB, (g) TVAL3 with 6.28 s and 19.37 dB, (h) CGDGI with 0.40 s and 19.38 dB. For all the algorithms, the iteration number is set to 10.

3.2. Experiments

In order to verify CGDGI's practical reliability, experiments were carried out at BL09B and BL13W1 beamlines of Shanghai Synchrotron Radiation Facility (SSRF), as shown in Fig. 4. The experiments were usually carried out at midnight to ensure the stability of the x-ray source and the minimum effect of the ground vibration. The energy of monochromatic x-ray beam was set to 15 keV to generate speckle patterns with violent fluctuations according to the property of alumina sandpaper as shown in Fig. 4(b). The FWHM and maximum of the autocorrelation function for all the speckle patterns are 72 μm and 1.26, respectively, as shown in Fig. 4(c). The FWHM of 72 μm which corresponds to the point-spread function (PSF) of traditional GI,[32] is consistent with the average particle size of 75 μm in the sandpaper. The sample for the experiments was placed 45 cm downstream of the sandpaper acting as the mask, followed by the panel detector (HAMAMATSU, ORCA-flash 4.0 C11440) which was located about 0.3 cm away from the object. Magnified with microscopic objectives of 2× or 10×, the effective pixel size of the panel detector is 3.25 μm or 0.65 μm respectively. Moreover, air-cooling was replaced with water-cooling to degrade the thermal noise introduced by the detector. High-contrast tungsten wire (TW) with 64×64 pixels and low-contrast sample of character '5' with 54×36 pixels in a resolution chart were selected as the experimental samples to verify the reliability of the proposed method for objects in different classifications. The speckle patterns in the reference arm and the signals in the object arm were collected in turn by toggling the object in and out of the x-ray beam.

In the experiment of tungsten wire, the exposure time for a single speckle pattern was set to 6 s, which depends on the flux density of incident x-ray, detector efficiency and mask absorption. Considering the bucket detector is synthesized by integrating the total intensity all over the pixels of the detector, exposure time in the object arm was also set to 6 s. Together with the time needed for the motor scanning, the average time required to collect a pair of data is 16 s. As a result, the total time for data acquisition of 660 measurements is 2.9 hours. As for object of character '5', the total time for the data-acquisition is 2.4 hours, in which the exposure time is 10 s with a 10× optical magnification and measurements of 360.

Due to the FWHM of 72 μm larger than wire's diameter 20 μm, traditional GI cannot retrieve the image of TW while the linear or CS algorithms could discern TW's structure, as shown in Fig. 5. Firstly, the linear algorithms including IDGI and PGI are employed to reconstruct the TW image with 550 measurements. The result of DGI is shown in Fig. 5(b) and the superposition of TW is fairly discriminated. IDGI improves the contrast of the wire but with lower SNR, as shown in Fig. 5(c). PGI retrieves the cross of the wire evidently as shown in Fig. 5(d). However, the image is severely deteriorated by the stochastic speckles, which implicates that PGI is hard to be employed for the reconstruction of natural sample with continuous and complex microstructures in noisy background. Accordingly, the linear algorithms are unable to implement XGI efficiently.

Instead of the linear algorithms, CS algorithms including OMP, BPDN, and TVAL3 are used for the image reconstruction. In the OMP image as shown in Fig. 5(e), the background wrinkles deform the image of wires significantly, which means

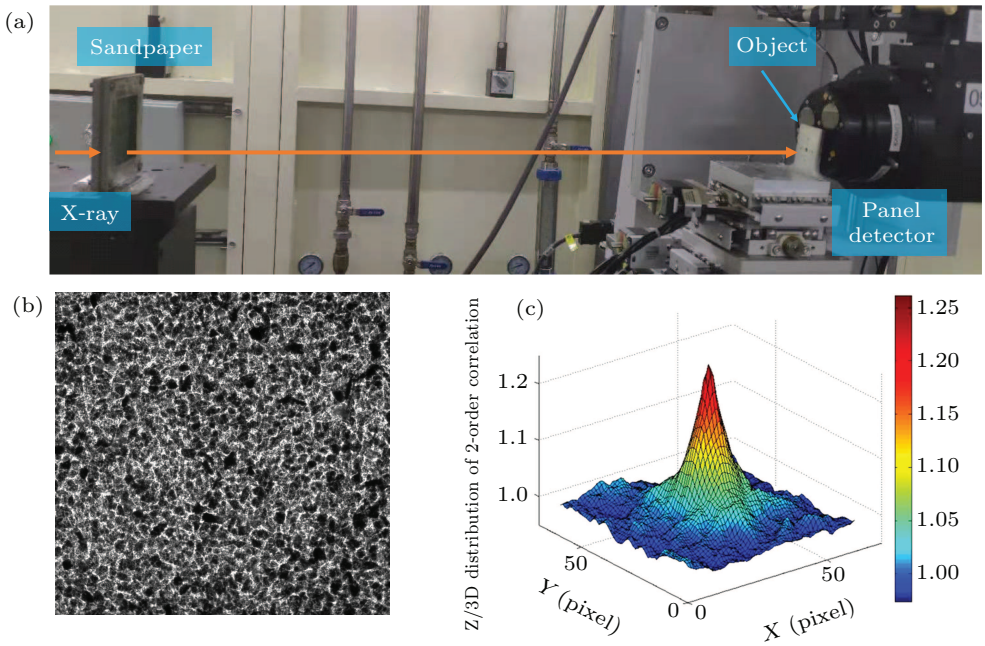


Fig. 4. Photographs for the experiments, where (a) experimental setup and (b) a speckle pattern in the reference beam, (c) autocorrelation of the speckle pattern in which the FWHM and maximum are 72 μm and 1.26, respectively.

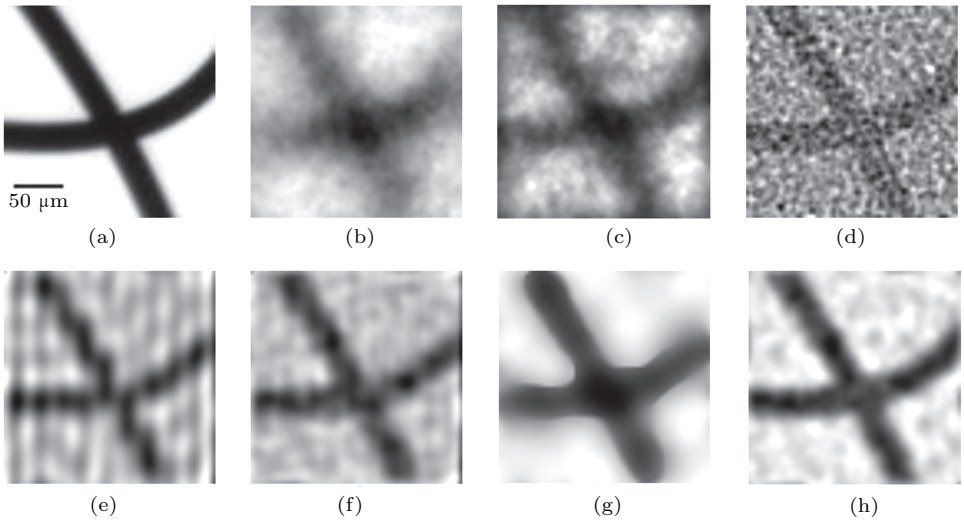


Fig. 5. TW reconstructed by various algorithms under 550 measurements: (a) target image, (b) DGI, (c) IDGI, (d) PGI, (e) OMP, (f) BPDN, (g) TVAL3, (h) CGDGI with the iteration number of 10 and λ set to 0.9.

the incapability of OMP for the efficient implementation of XGI. As shown in Fig. 5(f), the advantage of BPDN's noise resistance improves the SNR of the retrieved image obviously compared to that of OMP as shown in Fig. 5(e). However, the image background is still noisy to some extent. According to Fig. 5(g), TVAL3 retrieves the image with a smooth background, but also with an additional thickening of the wires especially at the superposition. The apparent thickening effect will reduce the fidelity of TVAL3 for the image reconstruction. Finally, CGDGI is employed to reconstruct the image of TW with λ set to 0.9 and the result is shown in Fig. 5(f). Compared to Figs. 5(d) and 5(g), the problems encountered by PGI and TVAL3 are overcome successfully by CGDGI and the best image quality among all the algorithms mentioned above are achieved according to the intuitive analysis. To compare effect of the algorithms quantitatively, PSNR, SSIM and MR are chosen to qualify the retrieved images and the results are listed in Table 1. Evidently, CGDGI gains the best value of the quality metrics against all the other algorithms. This implicates that CGDGI has the great potential for the efficient implementation of XGI. In addition, data processing efficiency of the algorithm is also critical to the implementation of ghost imaging. According to the value of RT listed in Table 1, the time needed by CGDGI is comparable to that of PGI but much less than TVAL3. Comprehensively, CGDGI is the best candidate for the efficient implementation of XGI.

Measurements required by XGI determines the data acquisition efficiency directly. Moreover, radiation dose is critical for XGI and fewer measurements is always anticipated. For all the CS based algorithms, RT and PSNR vs. number of measurements are calculated and exhibited in Fig. 6. According to Fig. 6(a), image RT for CGDGI is at the similar level with OMP and much less than that of BPDN and TVAL3. Furthermore, RT of CGDGI does not increase clearly with the measurements. PSNR is employed to pursue the optimized measurements for the algorithms. As shown in Fig. 6(b), for the algorithms except BPDN, the PSNR value increases with the measurements in general and flattens out while the measurements reach to a critical value. According to Fig. 6(b), CGDGI dominates the best PSNR among all the CS algorithms with the variation of measurements and its PSNR arrives at almost a maximum while the measurements reach to 550. The correspondent sampling rate is 13.4%, which implies that low radiation dose can be achieved by CGDGI. Comprehensively, owing to the advantages of high PSNR, rapid image reconstruction and low sampling rate, CGDGI is practicable for the efficient implementation of XGI. Moreover, low sampling rate of CGDGI signifies high efficiency in data acquisition and low radiation dose.

Table 1. Performances of different methods for tungsten wire with the measurements of 550.

Method	DGI	IDGI	PGI	OMP	BPDN	TVAL3	CGDGI
PSNR (dB)	11.60	8.32	8.24	12.09	13.34	15.15	15.85
SSIM	0.6663	0.5466	0.4423	0.7270	0.7854	0.8831	0.8878
MR	0.9564	0.9452	0.9344	0.9692	0.9736	0.9823	0.9856
RT (s)	0.012	0.470	0.344	0.073	2.994	6.112	0.213

Common samples for x-ray imaging are not pure absorption like tungsten wires. Therefore, a character '5' in a resolution chart (model: JIMA RT RC-02B) for x-ray imaging is taken to demonstrate the proposed method. The character '5' is made of 1 μm-thick tungsten film plated on a silicon base. Obviously, tungsten film with 1 μm thickness implies that character '5' is a low-contrast object. In the experiments, the character '5' in the resolution chart is imaged with a field of view of 54×36 pixels. The total measurement number is set to 360 which corresponds to the sampling rate of 18.5%. The effective pixel size of the detector used for the experiments is 0.65 μm and the average absorption of the object is 9%. To ensure the reliability of the signal containing the object information in the signal arm, the exposure time for each

frame is up to 10 s. Figure 7 shows the images of the character '5' retrieved by the linear and CS algorithms, with the target image supplied for comparison as shown in Fig. 7(a). The results of linear algorithms are shown in Figs. 7(b)–(d) respectively. It is no doubt that low contrast increases the difficulty of reconstruction, and none of the linear algorithm including DGI, IDGI and PGI can retrieve the contour of '5'. Then the CS based algorithms are employed to retrieve the object and the images are shown in Figs. 7(e)–7(h) respectively. From Fig. 7(e), the character of '5' cannot be figured out in the image reconstructed by OMP. BPDN can retrieve the profile of '5' but with a very noisy background, as shown in Fig. 7(f). At last, both TVAL3 and CGDGI could successfully restore the object, but CGDGI achieves higher image quality than TVAL3 with the coefficient λ set to 0.8, as shown in Figs. 7(g) and 7(h). As presented in the figure caption, the PSNR for CGDGI is 15.4 dB, e.g., the highest value among all the algorithms, which is consistent with the intuitive judgement. The RT of 0.04 s for CGDGI signifies the efficient image reconstruction of the proposed algorithm. As a result, for low-contrast objects, CGDGI could still obtain high-fidelity images with 1 to 2 orders of magnitude less time than the other CS algorithms, which demonstrates the applicability of the proposed method for low-contrast objects.

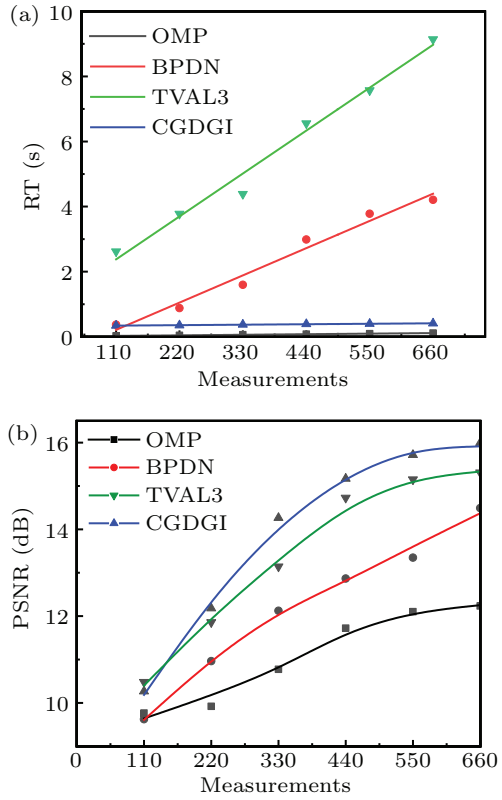


Fig. 6. Performance of CS algorithms versus measurements for the retrieval of TW, where (a) RT and (b) PSNR of CS algorithms including OMP, BPDN, TVAL3 and CGDGI.

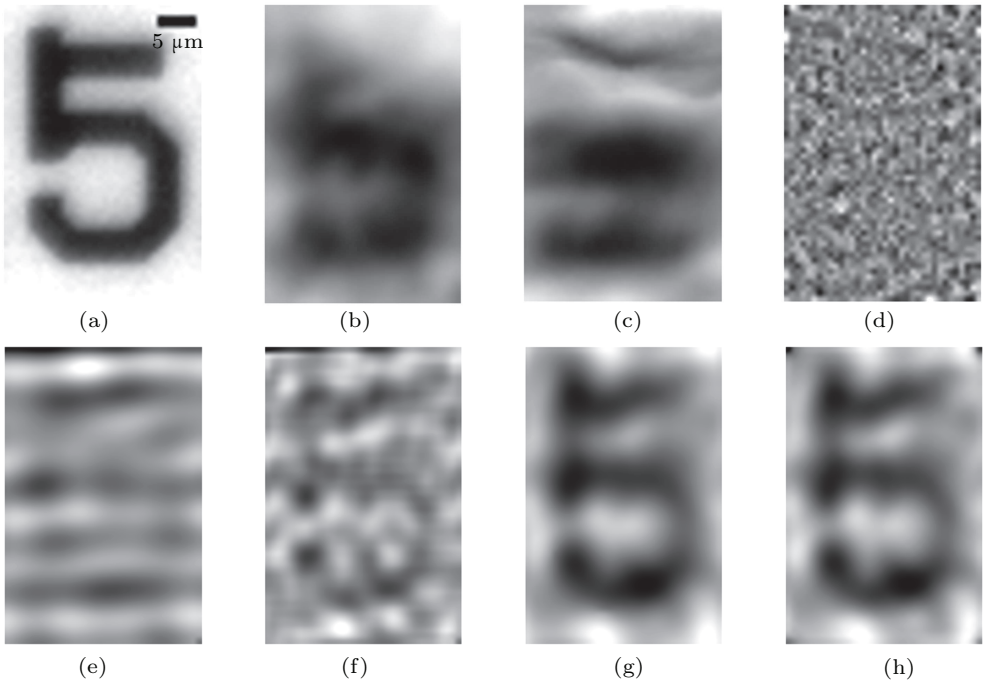


Fig. 7. Character '5' in the resolution chart is reconstructed by various algorithms with the measurement number $M = 360$: (a) target image, (b) DGI with RT of 0.01 s and PSNR of 9.91 dB, (c) IDGI with 0.10 s and 9.37 dB, (d) PGI with 0.13 s and 1.79 dB, (d) OMP with 0.03 s and 11.16 dB, (f) BPDN with 5.79 s and 12.19 dB, (g) TVAL3 with 2.83 s and 14.31 dB, (h) CGDGI with 0.04s and 15.40 dB with iteration number set to 10 and λ set to 0.8.

4. Conclusion and perspectives

Towards efficient implementation of x-ray ghost imaging, efficient data acquisition and fast image reconstruction together with high image quality are preferred. In view of radiation dose resulted by the incident x-rays, fewer measurements with sufficient SNR are always anticipated. Available linear and compressive sensing algorithms cannot meet all the

requirements simultaneously. In this paper, a method based on a modified compressive sensing algorithm, e.g., the so called CGDGI, is developed to solve the problem encountered in the efficient implementation of XGI. The conjugate gradient descent method is integrated into the CS algorithm to accelerate the reconstruction, which not only satisfies the sparse property of natural samples but also meet the inherent constraints.

To improve the reconstruction fidelity and meanwhile reduce the reconstruction time, image reconstructed by DGI is selected as the initial input of the iterations in CGDGI. Numerical simulation demonstrates that the image reconstruction time of CGDGI is significantly reduced to subsecond while the image quality is comparable to that of a typical CS algorithm called TVAL3. Experiments with high-contrast object demonstrate that owing to the advantages of high PSNR, rapid image reconstruction and low sampling rate in comparison to all the other linear and CS algorithms, CGDGI is practicable for the efficient implementation of XGI. Moreover, low sampling rate of CGDGI signifies high efficiency in data acquisition and low radiation dose. Experimental results of low-contrast object verify that CGDGI could still retrieve high-fidelity images with 1 to 2 orders of magnitude less time than the other CS algorithms, which further demonstrates applicability of the proposed method for low-contrast objects.

In conclusion, the CGDGI based method shows great potential in the efficient implementation of XGI. In general, the need of numerous measurements and tedious image reconstruction time is considered to be the main constraints in XGI for efficient and low-dose radiology compared to conventional imaging methods. The proposed method should be an effective solution for these problems encountered currently. The difficulty in manufacturing a dedicated spatial modulator for x-rays limits the direct use of computational imaging for XGI. Take sandpaper as the spatial modulator, collect the modulated patterns in reference arm with high resolution detector in advance, repeat the modulator scanning process and record the correspondent patterns very quickly in the signal arm with low resolution or bucket detector. Consequently, the efficiency in data acquisition of XGI can be improved significantly. After integrating these processes into the proposed CGDGI based method, x-ray ghost imaging to dynamic evolution in samples is also predictable.

Acknowledgements

The authors thank Yanan Fu, Han Guo, Guanyun Peng, Yanling Xue, Fen Tao, Zhijie Tan for their kind help and fruitful discussion on experiments and data processing.

Project supported by the National Key Research and Development Program of China (Grant Nos. 2017YFA0206004, 2017YFA0206002, 2018YFC0206002, and 2017YFA0403801) and National Natural Science Foundation of China (Grant No. 81430087).

References

[1] Ferri F, Magatti D, Gatti A, Bache M, Brambilla E and Lugiato L A 2005 *Phys. Rev. Lett.* **94** 183062
[2] Yu H, Lu R H, Han S S, Xie H L, Du G H, Xiao T Q and Zhu D M 2016 *Phys. Rev. Lett.* **117** 113901
[3] Huang Y Y, Ouyang C, Fang K, Dong Y F, Zhang J, Chen L M and Wu L A 2021 *Chin. Phys. B* **30** 064202
[4] Gatti A, Brambilla E, Bache M and Lugiato L A 2004 *Phys. Rev. Lett.* **93** 093602
[5] Zhang M H, Wei Q, Shen X, Liu Y F, Liu H L, Chen J and Han S S 2007 *Phys. Rev. A* **75** 021803
[6] Chen X H, Liu Q, Luo K H and Wu L A 2009 *Opt. Lett.* **34** 695
[7] Chen X H, Agafonov I N, Luo K H, Liu Q, Xian R, Chekhova M V and Wu L A 2010 *Opt. Lett.* **35** 1166
[8] Gong W L 2015 *Photon. Res.* **3** 234
[9] Meng S Y, Shi W W, Ji J, Tao J J, Fu Q, Chen X H and Wu L A 2020 *Chin. Phys. B* **29** 128704
[10] Oh J E, Cho Y W, Scarcelli G and Kim Y H 2013 *Opt. Lett.* **38** 682
[11] Kingston A M, Fullagar W K, Myers G R, Adams D, Pelliccia D and Paganin D M 2021 *Phys. Rev. A* **103** 033503
[12] Zhang A X, He Y H, Wu L A, Chen L M and Wang B B 2018 *Optica* **5** 374
[13] Pelliccia D, Rack A, Schell M, Cantelli V and Paganin D M 2016 *Phys. Rev. Lett.* **117** 113902
[14] Schori A and Shwartz S. 2017 *Opt. Express* **25** 14822
[15] Kingston A M, Pelliccia D, Rack A, Olbinado M P, Cheng Y, Myers G R and Paganin D M 2018 *Optica* **5** 1516
[16] Wang L and Zhao S M 2020 *Chin. Phys. B* **29** 024204
[17] Li E R, Chen M L, Gong W L, Wang H and Han S S 2012 *Journal of Electronics (China)* **29** 617
[18] Rizvi S, Cao J, Zhang K Y and Hao Q 2020 *Scientific Reports* **10** 11400
[19] Li Q, Duan Z T, Lin H Z, Gao S B, Sun S and Liu W T 2016 *Chin. Opt. Lett.* **14** 111103
[20] Klein Y, Schori A, Dolbnya I P, Sawhney K and Shwartz S 2019 *Opt. Express* **27** 3284
[21] Katz O, Bromberg Y and Siberberg Y 2009 *Appl. Phys. Lett.* **95** 131110
[22] Zhao S M and Zhuang P 2014 *Chin. Phys. B* **23** 054203
[23] Ferri F, Magatti D, Lugiato L A and Gatti A 2010 *Phys. Rev. Lett.* **104** 253603
[24] Li C 2011 *An efficient algorithm for total variation regularization with applications to the single pixel camera and compressive sensing* (Ph. D. dissertation) (Huston: Rice University)
[25] Wang J, Kwon S, Li P and Shim B 2016 *IEEE Transactions on Signal Processing* **64** 1076
[26] Chen S S, Donoho D L and Saunders M A 1998 *SIAM J. Sci. Comput.* **20** 33
[27] Martino D, Matias Flores J, Ayubi J L, Alonso G A, Fernandez J R, Ferrari A and Jose A 2012 *Appl. Opt.* **51** 3439
[28] Wang Z, Bovik A C, Sheikh H R and Simoncelli E P 2004 *Transactions on Image Processing (IEEE)* **13** 600
[29] Tang W J 2015 *Research on Compressed Sensing Reconstruction Algorithm and Its Application in Wireless Sensor Networks (MS dissertation)* (Nanjing: Nanjing University of Posts and telecommunications) (in Chinese)
[30] Yao X R, Yu W K, Liu X F, Li L Z, Li M F, Wu L A and Zhai G J 2014 *Opt. Express* **22** 24268
[31] Zhang C, Guo S X, Cao J S, Guan J and Gao F L 2014 *Opt. Express* **22** 30063
[32] Pelliccia D, Olbinado M, Rack A, Kingston A, Myers G and Paganin D M 2018 *IUCrJ* **5** 428
[33] Gao C, Wang X Q, Cai H J, Ren J, Liu J Y and Yao Z H 2019 *Chin. Phys. B* **28** 20201